Available online at ScienceDirect

Nuclear Engineering and Technology

journal homepage: www.elsevier.com/locate/net

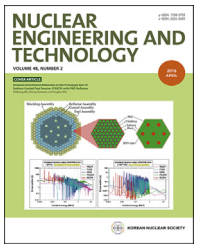

Original Article

Monte Carlo Analysis of the Accelerator-Driven System at Kyoto University Research Reactor Institute

Wonkyeong Kim [a], *Hyun Chul Lee* [b], *Cheol Ho Pyeon* [c], *Ho Cheol Shin* [d], *and Deokjung Lee* [a,*]

[a] *Nuclear Engineering Division, Ulsan National Institute of Science and Technology, 50 UNIST-gil, Ulsan 44919, Republic of Korea*

[b] *VHTR Technology Development Division, Korea Atomic Energy Research Institute, 111 Daedeok-daero 989 Beon-gil, Yuseong-gu, Dajeon 34057, Republic of Korea*

[c] *Nuclear Engineering Science Division, Kyoto University Research Reactor Institute 1010, Asahiro-nishi-2, Kumatori-cho, Sennan-gun, Osaka 590-0494, Japan*

[d] *Core and Fuel Analysis Group, Korea Hydro & Nuclear Power Central Research Institute (KHNP-CRI), 70 Yuseong-daero 1312 Beon-gil, Yuseong-gu, Daejeon 34101, Republic of Korea*

ARTICLE INFO

Article history:
Received 9 July 2015
Received in revised form
3 November 2015
Accepted 7 November 2015
Available online 17 December 2015

Keywords:
Accelerator-Driven System
Kyoto University Critical Assembly
Monte Carlo

ABSTRACT

An accelerator-driven system consists of a subcritical reactor and a controllable external neutron source. The reactor in an accelerator-driven system can sustain fission reactions in a subcritical state using an external neutron source, which is an intrinsic safety feature of the system. The system can provide efficient transmutations of nuclear wastes such as minor actinides and long-lived fission products and generate electricity. Recently at Kyoto University Research Reactor Institute (KURRI; Kyoto, Japan), a series of reactor physics experiments was conducted with the Kyoto University Critical Assembly and a Cockcroft–Walton type accelerator, which generates the external neutron source by deuterium–tritium reactions. In this paper, neutronic analyses of a series of experiments have been re-estimated by using the latest Monte Carlo code and nuclear data libraries. This feasibility study is presented through the comparison of Monte Carlo simulation results with measurements.

1. Introduction

An accelerator-driven system (ADS) is a design concept that comprises a subcritical reactor and a high-energy proton accelerator [1,2]. The reactor in the ADS needs an external neutron source to sustain fission chain reactions because it is operated in a subcritical state. In general, the external neutron source is provided by the spallation of a heavy nuclide such as

* *Corresponding author.*
E-mail address: deokjung@unist.ac.kr (D. Lee).
http://dx.doi.org/10.1016/j.net.2015.12.001

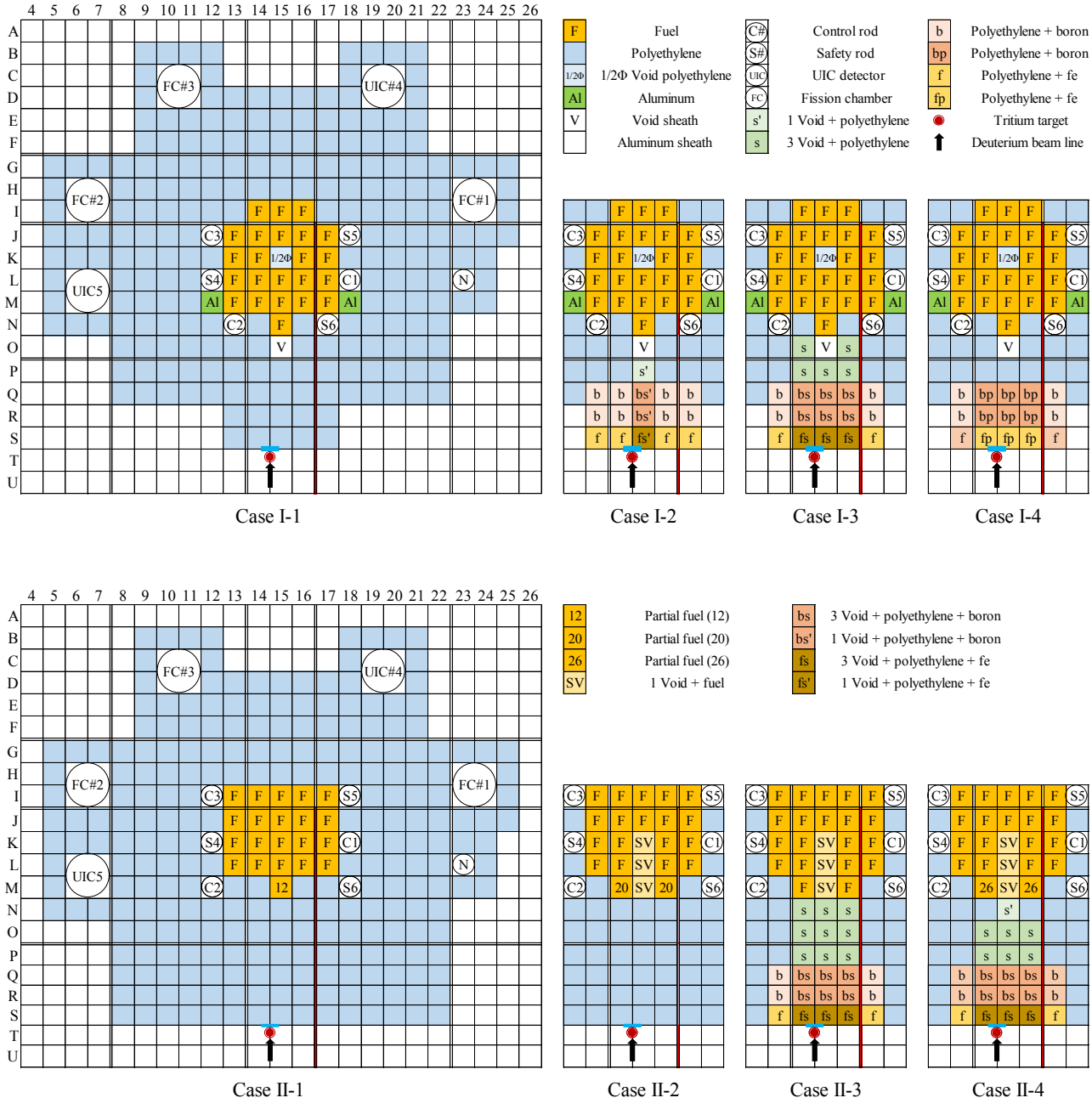

Fig. 1 – Plan view of the Kyoto University Critical Assembly Core configuration. Rods are indicated by "f", "b", "bs", "s", and "s′". F, normal fuel; N, neutron source; SV, special fuel.

lead (Pb) that is induced by a high-energy proton beam generated in an accelerator. Because the external neutron source is provided, flexible compositions and isotopes can be utilized in the ADS. Another feature of the ADS is that it can be used for effective transmutation of the minor actinides and long-lived fission products. However, the main advantage of ADS is in ensuring its own intrinsic safety when operated under subcritical conditions. The ADS can be stopped when the beam current supply into the accelerator is turned off so that it prevents a reactor from a supercritical accident. In March 2009, ADS experimental research at Kyoto University Research Reactor Institute (KURRI) was launched to establish measurement techniques for neutronic parameters with the use of the Kyoto University Critical Assembly (KUCA). A series of reactor physics experiments were performed by using the KUCA A-type core, which uses polyethylene as the moderator and reflector. The KUCA A-type core is combined with a Cockcroft–Walton type accelerator to generate an external neutron source. Instead of the neutron source being derived from the spallation of a heavy nuclide, a 14.1 MeV pulsed neutron beam produced by deuterium–tritium (D–T) fusion reactions is injected into the core where highly enriched uranium is loaded [3,4]. The neutronic parameters have been investigated in a series of KUCA experiments, and an

experimental benchmark for ADS KUCA has been launched to verify the measurements [4]. This study presents the Monte Carlo model of ADS KUCA to determine neutronic parameters such as reactivity, indium wire reaction rate distributions, and foil activation. This study also provides a good evaluation of the computational resources, the Monte Carlo code, and the cross-section libraries. The Monte Carlo N-Particle (MCNP) code is used to estimate the neutronic parameters. The MCNP code is a general purpose Monte Carlo code that can handle the coupled neutron/photon transport through a generalized three-dimensional geometry [5,6]. A versatile and accurate full model of the KUCA core is represented using the MCNP-6.1 code with continuous neutron energy data. A detailed description of the calculation model and the calculated parameters are provided in this paper. A comparative analysis of the measurements was performed using the calculation results of the MCNP-6.1 code with the continuous energy cross-section library (ENDF/B-VII.1 [7]), and with dosimetry libraries (IRDFFv1.05 [8] and JENDL/D-99 [9]). This analysis also allows validation of the MCNP code and three cross-section libraries against the KUCA A-type core by comparing the Monte Carlo solution with the measurements.

2. Description of the KUCA experiment

2.1. *Core configuration*

The KUCA A-type core, which is combined with the Cockcroft–Walton type pulsed neutron generator, employs polyethylene as the moderator and reflector. The A-core configurations consist of two series of experiments, each with four different cases. All eight cases of the A-core's configurations that were used to measure the reactivity and the indium wire reaction rate distribution are shown in Fig. 1 [3,4]. In addition, to obtain the neutron spectrum, the core configurations Case III-1, III-2, and III-3, derived from Case II-4, were used to measure the reaction rates of the activation foils. The core configurations Case III-1, III-2, and III-3 have the same configuration as Case II-4, except 20 fuel cells instead of 26 fuel cells are loaded in the partial fuel rod [10].

Each rod was composed of 2 inch (5.08 cm) square plates in a 0.15 cm thick aluminum sheath with an air gap of 0.025 cm between the material plate and the aluminum sheath, as shown in Fig. 2 [3,4]. In addition, there was an 0.05 cm thick outer air gap that encompassed the aluminum sheath so that the pitch of the rod was 5.53 cm. In all A-core configurations, 23 fuel rods were loaded. There are three different types of fuel: "F" is normal fuel; "SV" is special fuel; and "12", "20" and "26" are the partial fuels. The fuel rod "F" is composed of 36 fuel cells and polyethylene axial reflectors, as shown in Fig. 2. Each fuel cell is composed of a 1/4 inch (0.6300 cm) thick polyethylene plate, a 1/8 inch (0.3086 cm) thick polyethylene plate, and a 1/16 inch (0.1587 cm) thick highly (93%) enriched uranium–aluminum (U–Al) alloy plate. The "SV" fuel rod has 32 fuel cells, 5.0 cm thick void region at the middle of the fuel region, and axial reflectors. The void region has a 5.0 cm × 5.0 cm × 5.0 cm aluminum sheath with a thickness of 0.2 cm instead of 2 inch plates. The partial fuel rods "12", "20", and "26" have 12 fuel cells, 20 fuel cells, and 26 fuel cells, respectively, in the fuel region. In these partial fuels, the length of the polyethylene layer is conserved, as are those of "F". Therefore, in each partial fuel, the decreased height of fuel region is compensated for by adding Al cells composed of an Al plate and polyethylene plates at the top and bottom of the rod. The radial reflector rod (sky blue in Fig. 1), the "Al" rod, and "V" rod are filled with polyethylene, aluminum, and a void in the aluminum sheath, respectively. The "1/2Φ" rod is a hollow polyethylene rod with a 1.27 cm diameter hole at the center of the rod. Three fission chambers (FCs) and three detectors (UIC)

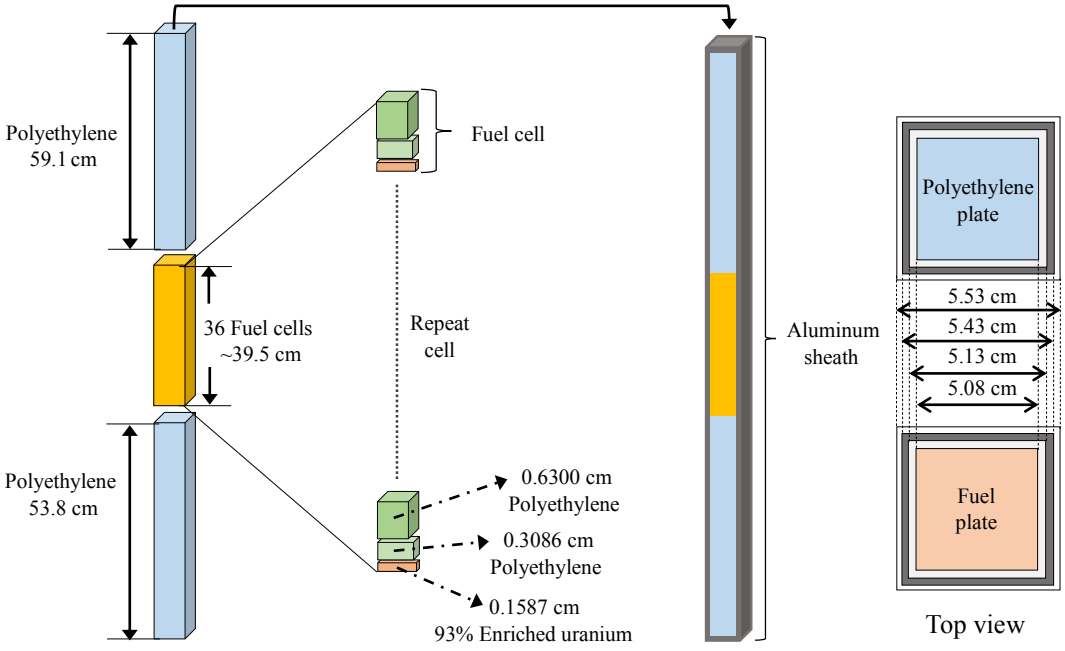

Fig. 2 – An illustration of the "F" fuel rod.

for reactor control and monitoring, and the neutron source (N) rod are around the perimeter of the core. An indium wire with a diameter of 0.15 cm is established along a line parallel to the y-axis of the core from the core center (16–17, J) to the target (16–17, U) at 78.9 cm from the top surface of the top reflector (z = −78.9 cm). The total height of the core, including the axial reflectors, is approximately 150 cm and the height of the active core is approximately 40 cm.

2.2. *Pulsed neutron generator specification*

The 14.1 MeV pulsed neutrons generated from the D–T fusion reactions are injected into the core through the polyethylene reflector. The deuteron beam is led to the tritium target outside the polyethylene reflector. The beam peak intensity is approximately 0.5 mA for a pulse width of up to 100 μs and the repetition rate varies from a few Hz to 30 kHz, providing up to 1×10^8 n/s [3,4].

2.3. *Neutron guide—neutron shield and beam duct*

The neutron shield and the beam duct shown in Fig. 3 are installed in the polyethylene reflector region of the cores, as shown in Fig. 1. The main purpose of installing the neutron shield and the beam duct was to induce the highest possible number of high-energy neutrons generated in the target into the center of the core. For shielding the high-energy and thermal neutrons, the neutron shield comprises several materials: iron (Fe) is used for shielding high-energy neutrons generated in the target region by inelastic scattering reactions; polyethylene containing 10 wt% boron for shielding thermal neutrons in the reflector region; and the beam duct (i.e., the void) for directing collimated high-energy neutrons by the streaming effect to the core region. Rod "b" is the neutron shield, which has 10 wt% boron in the middle of the rod. Rod "bs" has a similar shape as rod "b", but it has three void sheaths as beam ducts in the middle of the rod. Rod "bs'" also has one void sheath in the middle of the rod. Rods "f", "fs" and "fs'" have iron (Fe) in the middle of the rod. Rods "fs" and "fs'" have three void sheaths and one void sheath, respectively. Rods "fp" and "bp" have polyethylene in the middle of iron and boron, respectively, as shown in Fig. 3. Rods "s" and "s'" are the beam duct rods that consist of polyethylene and void sheaths in the middle of the rod. The control and safety rods consist of anhydrous boron with a diameter of 3.38 cm, which is surrounded by two layers of aluminum sheath, and contain an air gap between the layers. References [3,4, and 11] give detailed specifications of the experiments.

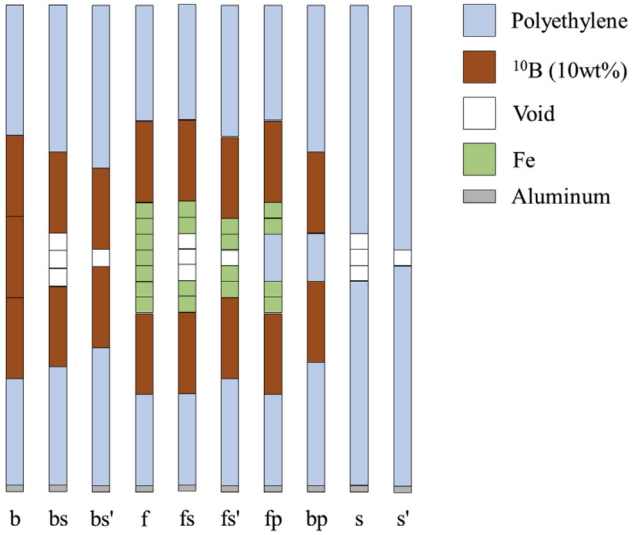

Fig. 3 – Description of the neutron shield and beam duct.

3. The MCNP Model

The KUCA core configurations were modeled and analyzed using the MCNP-6.1 code system and the continuous energy cross-sections of the ENDF/B-VII.1 library. This model explicitly describes the geometry of the KUCA core without any homogenized region. All configurations and detailed components were based on the benchmark specification from KURRI [3]. There is some missing information in the benchmark specifications: the description of the UIC detectors; "FC" (i.e., fission chamber); and "N" (i.e., neutron source). These are substituted with void sheaths, as shown in Fig. 4. To examine the effects of the substitution, two test calculations with configuration Case I-1 were performed before the main calculations. In the first test model, these regions were replaced with fuel rods instead of real structures, and the second model employs void sheath (V) in these regions. The control and safety rods were withdrawn in both models. In the calculations, 0.4 billion neutron histories, 300 active cycles, and 100 inactive cycles were used. The discrepancy in the effective multiplication factors of the two test models was only 15 pcm with a standard deviation of 8 pcm. Therefore, UIC, FC, and N in Fig. 1 were replaced with only V in the actual MCNP models. Several foils were placed in the core center region in Case II-2, Case 3, and Case 4 configurations, as shown in Fig. 5. Figs. 6 and 7 show the plan view of all core configurations at 78.9-cm from the top surface of the top reflector (z = −78.9-cm).

3.1. *Reactivity calculations*

The reactivity, which characterizes the deviation of the reactor from the critical state, was calculated for all core configurations shown in Figs. 6 and 7. The reactivity calculations were performed using MCNP-6.1 with the ENDF/B-VII.1 cross-section library. Excess reactivity was calculated under the condition that all control and safety rods were fully withdrawn. Subcriticality was calculated under the condition that all control rods were fully inserted. The positions of the control and safety rods in the critical state of each case are listed in Table 1 [3]. The configuration for the control rods and safety rods in the core is shown in Fig. 8. All calculations by MCNP-6.1 were performed with a total number of 3×10^8 neutron histories using 200 active cycles and 100 inactive cycles.

3.2. *Indium wire reaction rate distribution*

The calculations of the ^{115}In $(n,\gamma)^{116m}$In reaction rate distribution is performed in all cases in series I and series II in which an indium wire is set up along a line parallel to the y-

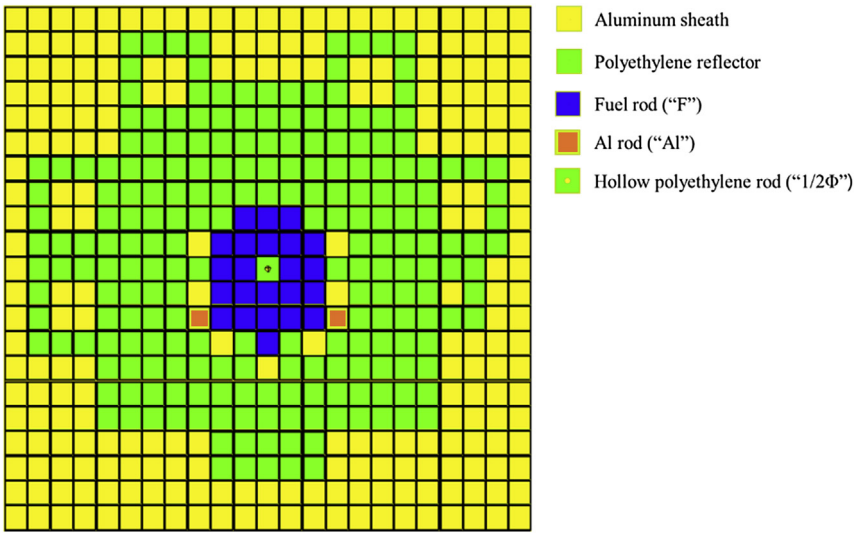

Fig. 4 – Plan view of the Monte Carlo N-Particle model for Case I-1.

axis from the target region to the center, as represented in Fig. 9. These calculations were performed by using a fixed-source calculation with 60 million neutron histories and using the F4 tally, which was associated with the FM4 card on reaction. A point neutron source of 14.1 MeV was used in the target region.

3.3. *Reaction rates of the activation foils*

The reaction rate of the activation foils was calculated using MCNP6.1 code. The nuclear data library used was the ENDF/B-VII.1 continuous energy cross-section library, and the IRDFFv1.05 and JENDL/D-99 dosimetry libraries. Calculation of the reaction rate in each foil was tallied using the F4 tally to investigate the effect of the use of the dosimetry library. Sixty million neutron histories were used in the fixed-source calculation. In these calculations, some different reaction type numbers (MT) on activation foils were used in the FM4 card when only the ENDF/B-VII.1 library was used or when it was used in combination with the IRDFFv1.05 or JENDL/D-99 dosimetry library. Two sets of foils were irradiated: one in the core center region (15, K) and the other around the target region. The arrangement of activation foils in the core center and at the target region is shown in Fig. 10. The values in parenthesis written on the foils indicate the thickness of the foil. The same 14.1 MeV point neutron source was used as in the indium wire reaction rate calculation.

4. Results

4.1. *The reactivity calculation for the KUCA core*

The criticality calculations for the core configurations in Case I and II were performed before the excess reactivity and sub-criticality calculations. Table 2 shows the criticality calculation results with the control rod positions in Table 1. An overestimation of the effective multiplication factors occurred for all core configurations. The excess reactivity and the sub-criticality were then calculated for all the core configurations

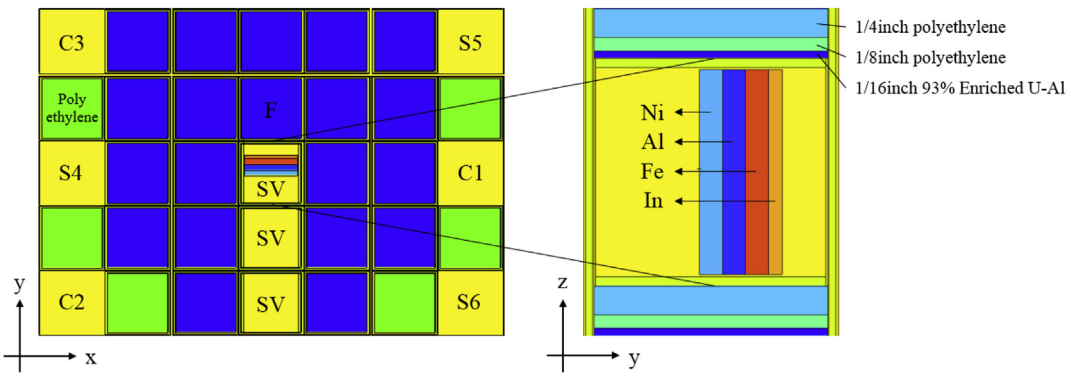

Fig. 5 – The Monte Carlo N-Particle model of the activation foil on the core center (15, K) of Case II-2, Case 3, and Case 4. Al, aluminum; C1–C3, control rods; Fe, iron; In, indium; Ni, nickel; SV, special fuel; S4–S6, safety rods; U, uranium.

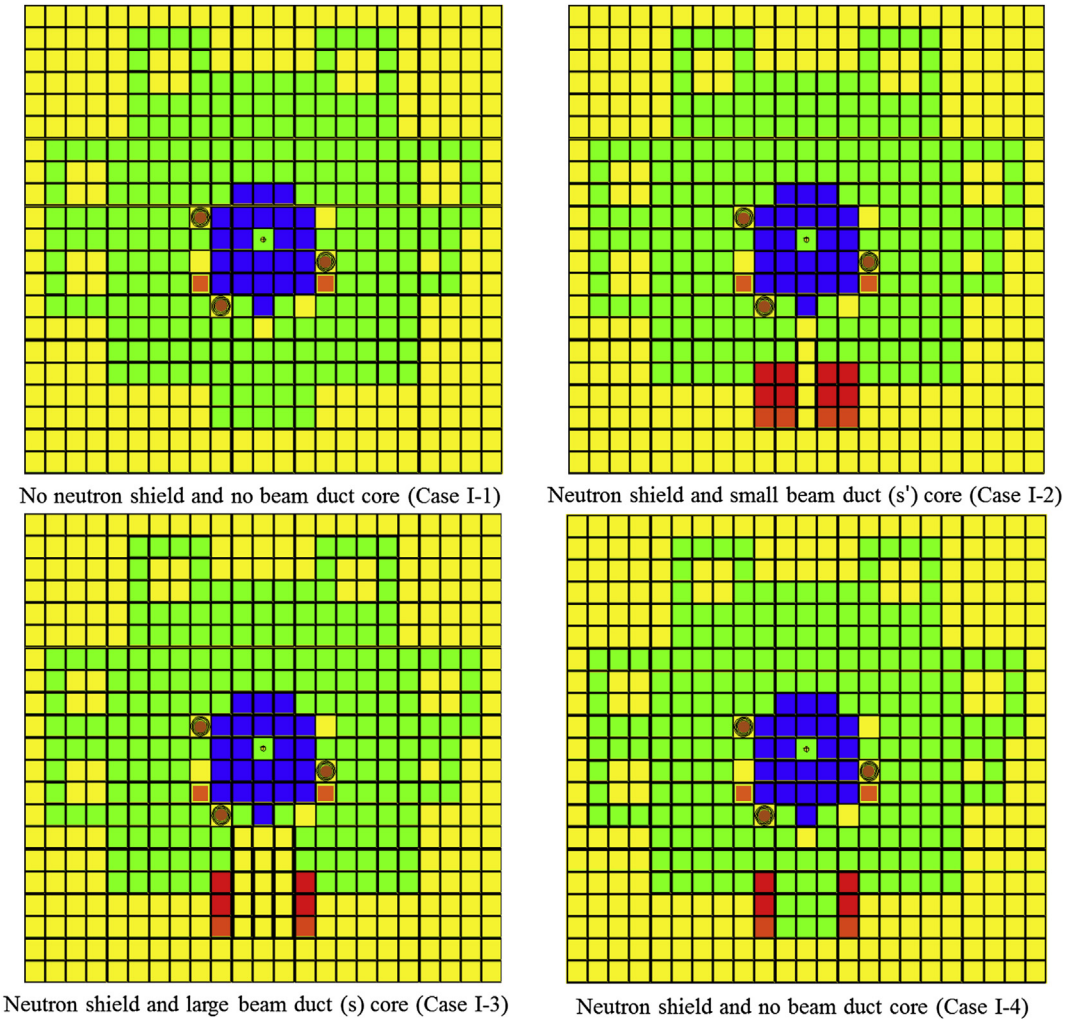

Fig. 6 – Monte Carlo N-Particle model of series I (the *x*–*y* view at *z* = −78.9 cm from the top of the core).

using Equation (1). The results are listed in Table 3 and compared with measurements given as benchmark specifications by KURRI [3].

$$\rho = \frac{k - k_{\text{critical}}}{k \times k_{\text{critical}}} \times 100 \quad (1)$$

For the excess reactivity calculation, relative errors were within 9%, except for Cases I-3 and II-3 for which the reactivity was very small and had large relative errors, even though the absolute error was quite small. On the other hand, the result of the subcriticality shows that the relative errors ranged between 3.6% (minimum) and 12.4% (maximum). These values are acceptable with regard to the experimental error and the statistical error in the simulation result.

4.2. *Reaction rate distribution on the indium wire*

For measuring the reaction rate distribution, indium wire is placed in the core along the position marked in Fig. 9. ^{115}In-dium has a high thermal neutron capture cross-section and is activated by a neutron to the form ^{116m}In with a half-life of 54 minutes. Before calculating the indium reaction rate distribution in the subcritical state, the atomic number density of uranium-235 (^{235}U) was adjusted (as shown in Table 4) to make the cores critical with the control rod positions listed in Table 1. In the subcritical fixed-source mode calculation for the estimation of the indium wire reaction rate distribution, the adjusted atomic number density of ^{235}U was used (Table 4). The same correction was thereafter applied to the subcritical state of all other cores and the corrected core configurations were used to calculate the reaction rate distribution [10]. The results of the comparison of the experimental values, which were estimated by KURRI, and the relative error are shown in Figs. 11–18. The results are normalized by dividing the reaction rates with the normalization factor defined in Equation (2):

$$f = \sum_{i=1}^{4} \sum_{j=1}^{30} r^{j}_{\text{Case I–i or Case II–i}} \quad (2)$$

in which f is the normalization factor, r is the reaction rate, i is the case number, and j is the index for the position of the measured and calculated reaction rate.

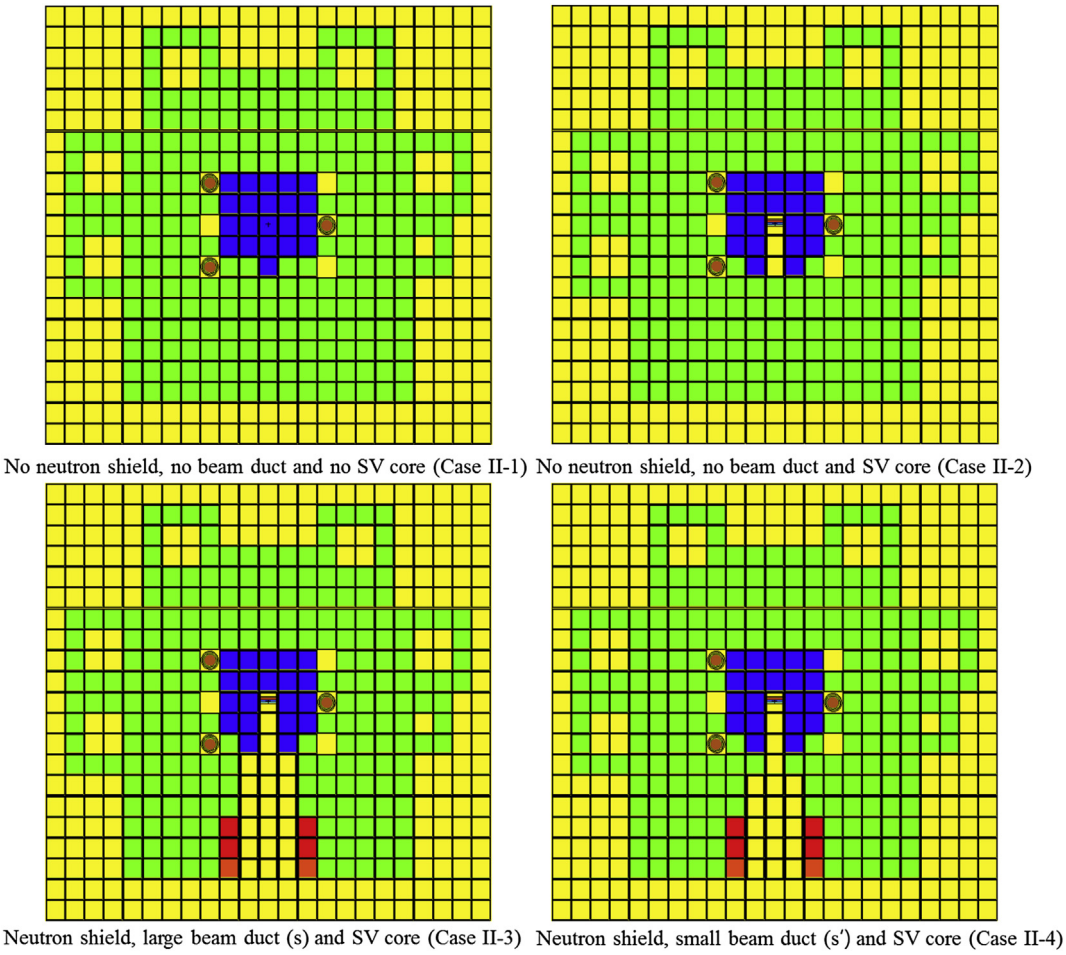

Fig. 7 – The Monte Carlo N-Particle model of series II (*x*–*y* view at *z* = −78.9 cm from the top of the core).

The measured and calculated reaction rate distributions for all core configurations showed good agreement with regard to the experimental error and statistical error in the simulation. Fig. 19 summarizes the ratios of the calculated value to the experimental data (i.e., C/E values) shown in Figs. 11–18. Most values in the fuel region had errors within 10%. In the reflector region, most calculated reaction rates were underestimated, compared to the measured reaction rates. The cause of the underestimation in the reflector region remains unclear and should be investigated carefully.

Table 1 – Control rod and safety rod position in all cases in the critical state.

Configuration	C1 (cm)[a]	C2 (cm)	C3 (cm)	S4–S6 (cm)
Case I-1	−21[b]	−21	−88.566	−21
Case I-2	−21	−21	−86.179	−21
Case I-3	−21	−21	−66.446	−21
Case I-4	−21	−21	−88.448	−21
Case II-1	−21	−21	−77.406	−21
Case II-2	−77.252	−21	−21	−21
Case II-3	−21	−21	−66.752	−21
Case II-4	−21	−21	−85.676	−21
Case III-1	−21	−21	−68.465	−21
Case III-2	−21	−21	−68.264	−21
Case III-3	−21	−21	−71.589	−21

[a] The origin (i.e., z = 0) is the top of the core.
[b] The position when the rod is fully withdrawn. C1–C3, control rods 1–3; S4–S6, safety rods 4–6.

The measured and calculated reaction rate distributions showed the effect of the beam duct, which promoted the transfer of high-energy neutrons into the fuel region. The configuration Case I-1 was the reference core configuration of Case I and had no beam duct, whereas a small beam duct was installed with neutron shielding in Case I-2. The beam duct was much larger in Case I-3 than in Case I-2. Fig. 12 in comparison with Fig. 11 shows that the effect of the small beam duct on the indium wire reaction rates in the fuel region was marginal, whereas the indium wire reaction rate in the reflector region was considerably reduced by the effect of the neutron shielding. Fig. 13 clearly shows that the large beam duct strictly increased the indium wire reaction rates in the fuel region. A similar trend occurred in Case II. The small beam duct concentrated the high-energy neutron beam on the center of the core, especially on column 15 in Fig. 1, whereas the large beam duct spread the neutron beam on the overall fuel region, especially on columns 14–16, which increased the reaction rate of the indium wire between column 16 and

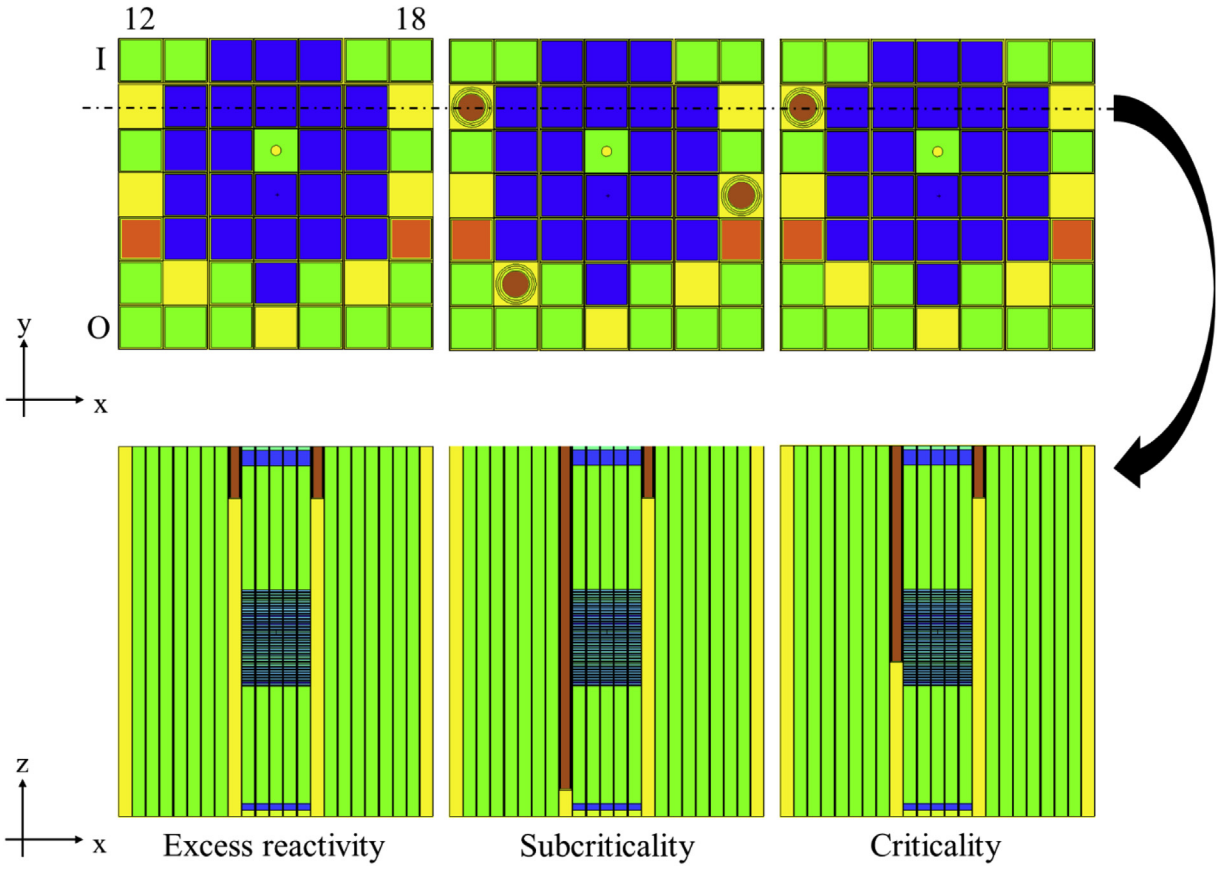

Fig. 8 – Configurations of the control and safety rods in three states (Case I-1).

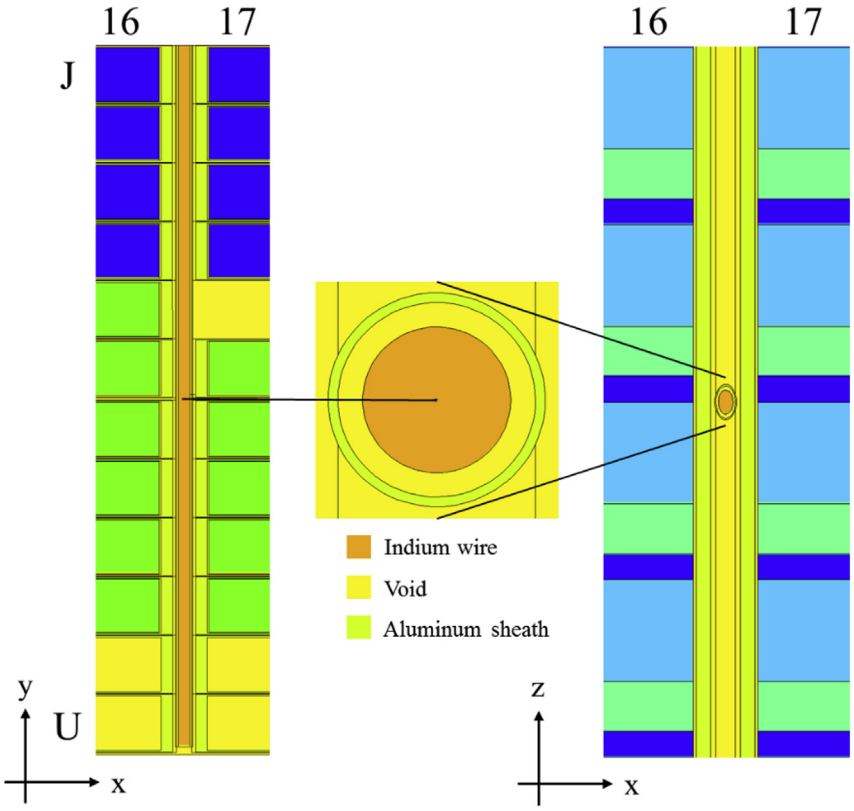

Fig. 9 – Configuration of the indium wire in core (Case I-1).

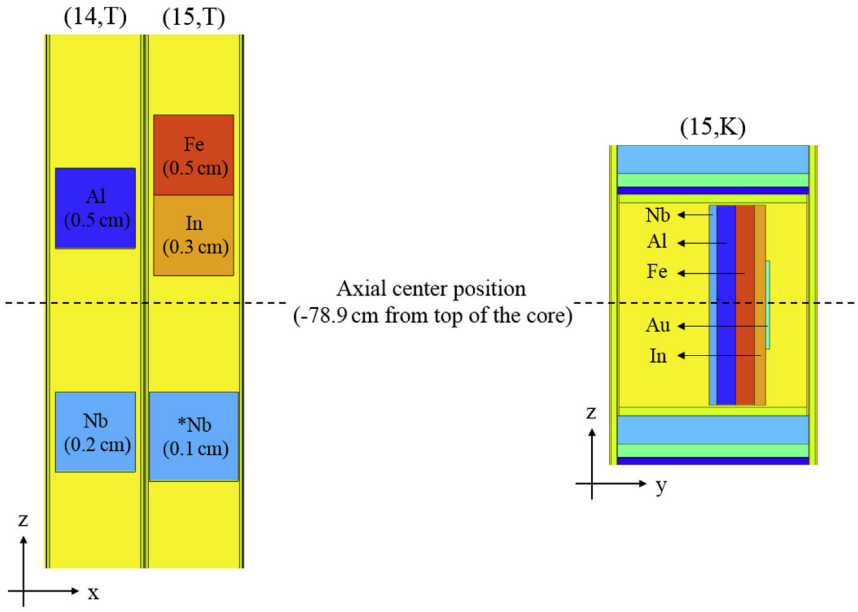

Fig. 10 – Configuration of foils in the target region (left) and the core center region (right) of Case III core. Al, aluminum; Au, gold; Fe, iron; In, indium; Nb, niobium; Ni, nickel.

column 17. The concentration of the high-energy neutron beam on column 15 can be confirmed by checking the neutron spectrum at the center of the core. Fig. 20 shows the high-energy neutron spectrum at (15, K) for the cores in Case I. More of the high-energy neutron beam reached the center of the core in the small beam duct case (i.e., Case I-2).

Fig. 21 shows the high-energy neutron spectrum at (15, K) for the cores in Case II. The small beam duct in the fuel region of Case II-2, denoted as "SV" in Fig. 1, increased the high-energy neutron flux at the center of the core. The large beam duct in the reflector region in Case II-3 greatly increased the high-energy neutron flux at the center of the core. However, the bottle-neck shape of the beam duct in Case II-4 obstructed the high-energy neutron beam. The high-energy neutron flux at the center of the core in Case II-4 was slightly lower than that in Case II-3.

4.3. *Reaction rates of the activation foils*

A comparison of the reaction rates of the activation foils was performed with C/E values [3]. As shown in Table 5, the calculated subcriticality values were in good agreement with the measured subcriticality values within 10% error in three core configurations (i.e., Case III-1, Case 2, and Case 3) used in this foil activation calculation. Before performing fixed-source calculation by MCNP6.1 code, as in the indium reaction rate calculation, the atom density of ^{235}U was artificially decreased by 2.5% to calibrate the overestimated effective multiplication factors so that the effective multiplication factor was equivalent to 1.00005 ± 0.00006. The adjusted atomic number density was used in the subcritical fixed-source mode calculation for the estimation of the foil activation.

Table 2 – The effective multiplication factor for the Kyoto University Critical Assembly cores.

Core	$k_{critical}$	σ	Error ($k_{critical}$ −1)
Case I-1	1.00423	0.00006	0.00423
Case I-2	1.00392	0.00005	0.00392
Case I-3	1.00377	0.00006	0.00377
Case I-4	1.00417	0.00006	0.00417
Case II-1	1.00610	0.00006	0.00610
Case II-2	1.00583	0.00006	0.00583
Case II-3	1.00484	0.00006	0.00484
Case II-4	1.00684	0.00006	0.00684

Table 6 shows the C/E values of the foil activities at the target region with the threshold energy of the activation reactions. The threshold energy of the activation reactions ranged 0.32–9.05 MeV. The activities of the foils at the target region were normalized with respect to that of niobium (*Nb) foil (Fig. 10). Table 6 shows that the underestimated activity of Fe and Al foils can be improved when the dosimetry libraries (i.e., IRDFFv1.05 and JENDL/D-99) are used with the ENDF/B-VII.1 library. Table 7 shows the C/E values of the foil activities at the core region normalized with respect to that of gold (Au) foil in Fig. 10. Fig. 22 plots the results listed in Table 7. The C/E values for Fe and Al activation with the three libraries agree well with each other, even though they are far from 1.0 except for some cases. On the contrary, the C/E values for In and Nb activation with ENDF/B-VII.1 library were much larger than the C/E values with the IRDFFv1.05 or JENDL/D-99 library. Fig. 23 plots the cross-sections of the activation reactions from the ENDF/B-VII.1 and JENDL/D-99 library normalized with respect to that from the IRDFFv1.05 library. For In and Nb activation cross-sections, large discrepancies existed between the cross-sections of the ENDF/B-VII.1 library and the IRDFFv1.05 library, but good agreement existed between JENDL/D-99 and IRDFFv1.05 libraries. This explains the large

Table 3 – The excess reactivity and subcriticality for Kyoto University Critical Assembly cores.

Core	Excess reactivity (%Δρ)[a]			Subcriticality (%Δρ)[b]		
	Experiment	Calculation	Relative error (%)	Experiment	Calculation	Relative error (%)
Case I-1	0.295 ± 0.021	0.297 ± 0.008	−0.7	−0.904 ± 0.063	−0.817 ± 0.008	9.7
Case I-2	0.293 ± 0.021	0.292 ± 0.008	0.3	−0.925 ± 0.065	−0.827 ± 0.008	10.6
Case I-3	0.020 ± 0.001	0.030 ± 0.008	−50.0	−1.171 ± 0.082	−1.026 ± 0.009	12.4
Case I-4	0.296 ± 0.021	0.296 ± 0.008	0.1	−0.907 ± 0.063	−0.815 ± 0.007	10.2
Case II-1	0.143 ± 0.010	0.156 ± 0.008	−8.9	−0.793 ± 0.056	−0.695 ± 0.009	12.4
Case II-2	0.246 ± 0.017	0.252 ± 0.008	−2.6	−0.677 ± 0.047	−0.627 ± 0.009	7.4
Case II-3	0.037 ± 0.003	0.052 ± 0.008	−40.5	−0.893 ± 0.063	−0.861 ± 0.009	3.6
Case II-4	0.232 ± 0.016	0.222 ± 0.008	4.5	−0.702 ± 0.049	−0.645 ± 0.009	8.1

[a] The control (C1, C2, and C3) and safety rods (S4, S5, and S6) are fully withdrawn.
[b] The control rods (C1, C2, and C3) are fully inserted.

Table 4 – The adjusted atom density of ^{235}uranium and the effective multiplication factors.

Configuration	Adjustment factor[a]	k_{eff}
Case I-1	0.9810	1.00008 ± 0.00006
Case I-2	0.9815	1.00004 ± 0.00006
Case I-3	0.9822	0.99998 ± 0.00006
Case I-4	0.9800	0.99992 ± 0.00006
Case II-1	0.9700	1.00001 ± 0.00006
Case II-2	0.9720	0.99996 ± 0.00006
Case II-3	0.9800	0.99996 ± 0.00006
Case II-4	0.9665	0.99995 ± 0.00006

[a] The adjusted atom density of ^{235}uranium (^{235}U)/the original atom density of ^{235}U.

C/E values for In and Nb activation with ENDF/B-VII.1 library. In the MCNP simulation, it is difficult to choose the correct cross-section for higher excited states [12]. That point also can be the cause of uncertainty of the C/E value for In foil. Tables 6 and 7 also show that the error between the measurement and the calculation is much larger in the core region than in the target region. The large void region in the core center induced by the installation of the neutron guide and the beam duct may increase the uncertainty in the experimental analyses [4,11]. In addition, the large size of activation foils was employed to attain a large number of γ-ray emission counts at the void region (15, K) at the center of the core because the normal operating power was very low because of the characteristics of the KUCA. It also caused in additional to uncertainty factors (e.g., self-shielding and source volume [10]). The C/E values for Fe foil activation are much lower than 1.0 and these large discrepancies were caused by impurity in the Fe foil, and were improved by using high purity Fe foil [13].

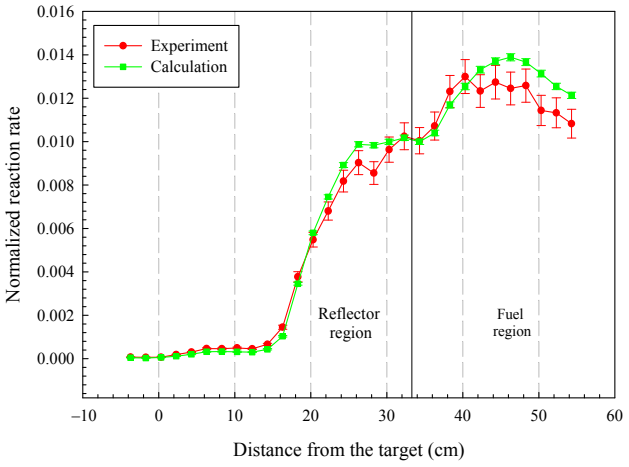

Fig. 12 – The reaction rate distribution of Case I-2.

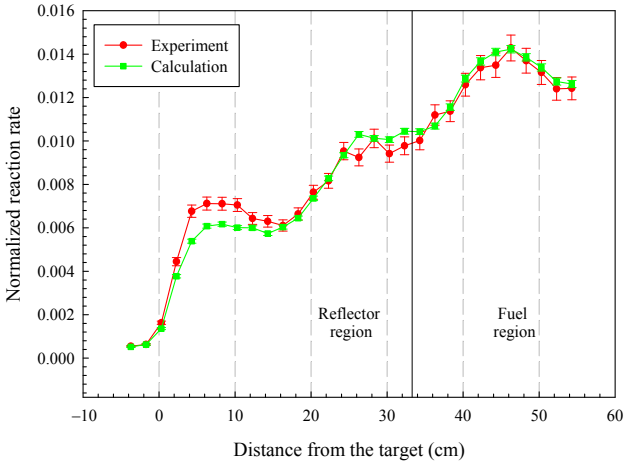

Fig. 11 – The reaction rate distribution of Case I-1.

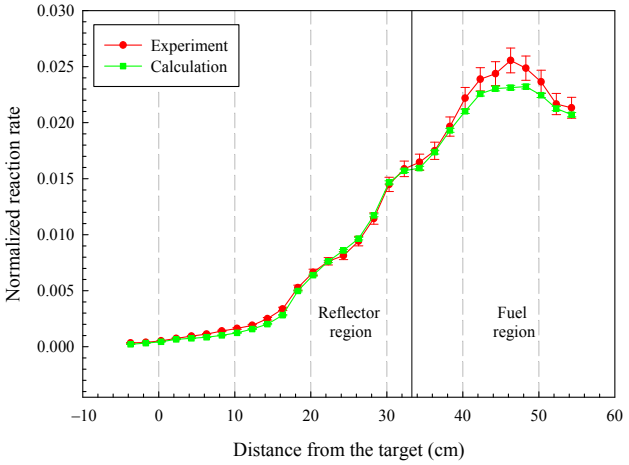

Fig. 13 – The reaction rate distribution of Case I-3.

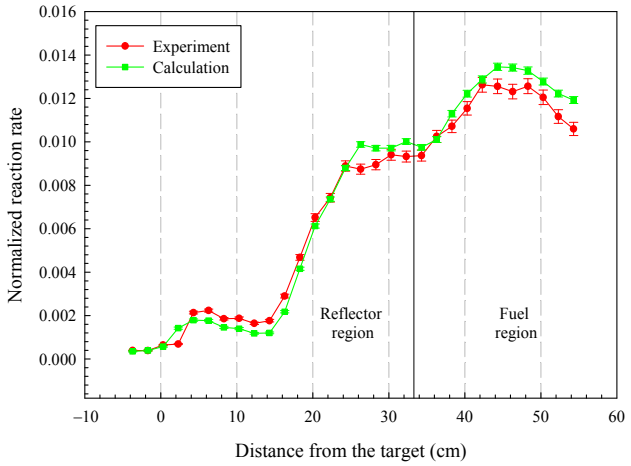

Fig. 14 – The reaction rate distribution of Case I-4.

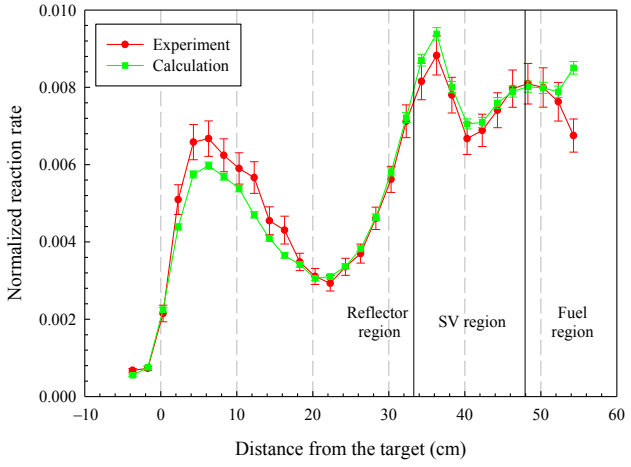

Fig. 15 – The reaction rate distribution of Case II-1.

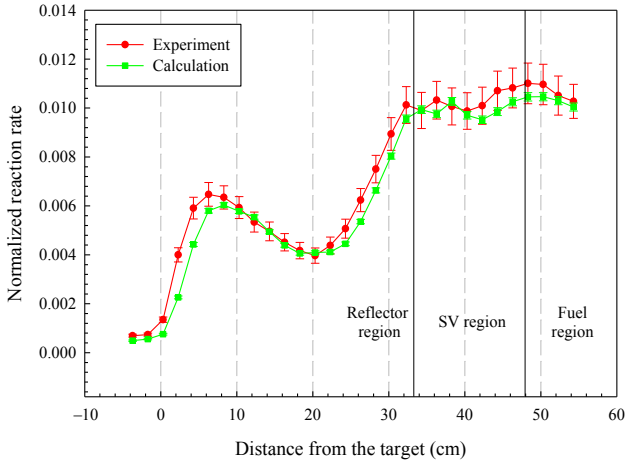

Fig. 16 – The reaction rate distribution of Case II-2. SV, special fuel.

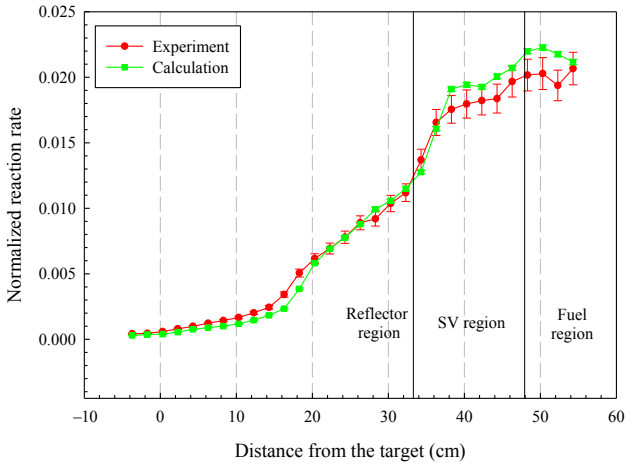

Fig. 17 – The reaction rate distribution of Case II-3. SV, special fuel.

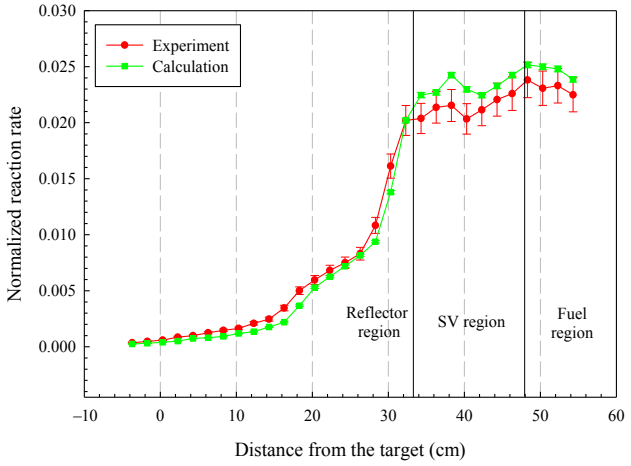

Fig. 18 – The reaction rate distribution of Case II-4. SV, special fuel.

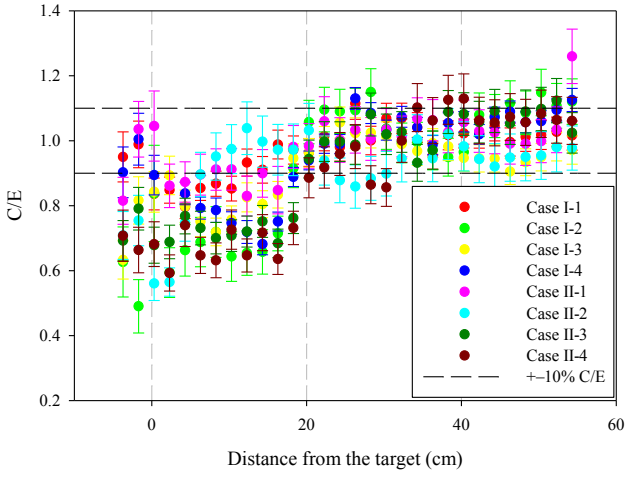

Fig. 19 – The C/E value for the reaction rate distribution. Calculation/Experiment (C/E).

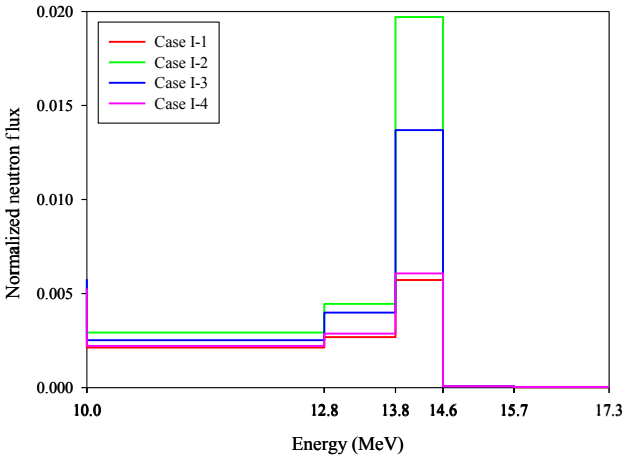

Fig. 20 – Neutron spectrum for Case I core configuration in the core region (15, K).

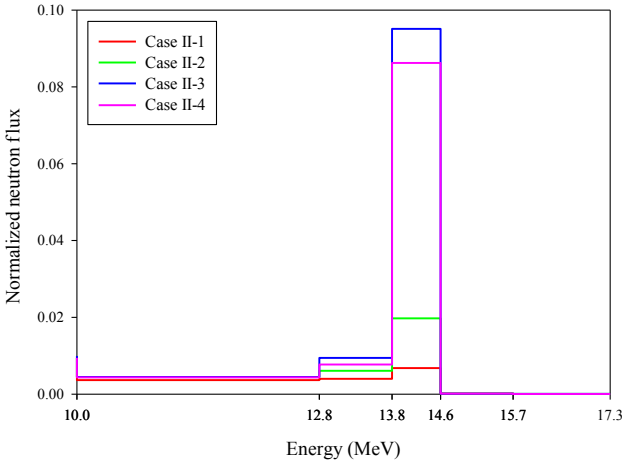

Fig. 21 – Neutron spectrum for Case II core configuration in the core region (15, K).

5. Discussion

The Monte Carlo analysis of the KUCA ADS experiments was conducted using MCNP-6.1, and new solutions were produced with ENDF/B-VII.1, JENDL/D-99 and IRDFFv1.05 nuclear data libraries. All core configurations were modeled according to benchmark specifications, and the calculation results were compared with the experimental values. The results of this benchmark analysis can be summarized as follows:

First, the reactivity calculations showed acceptable agreement with the measured values within a 9% error range for excess reactivity, and an error range from 3.6% to approximately 13% for subcriticality.

Second, the indium wire reaction rate along the core was calculated, and the result showed good agreement with the measured value. An increase in the reaction rate at the fuel region by installing a large beam duct and a decrease in the reaction rate at the reflector region because of neutron shield were observed, as in the experiment. When a small beam duct was installed, the high-energy neutron beam was concentrated on the core center. These effects were also confirmed by the neutron spectrum calculation in the core center region (15, K).

Third, foil activation calculations were performed using MCNP6.1 with only the transport cross-section library and by adding dosimetry libraries. Several types of foil activation, which covered a wide energy range, were calculated in the target and core regions and compared with the experimental value employing the C/E value. The C/E values for the target region clearly showed that using a dosimetry library improves the accuracy of the activation calculations by MCNP6.1. By contrast, the C/E values for the core region were far from 1.0, except for some cases, even when dosimetry data libraries were used in the calculation. The inaccuracy of cross-section libraries may cause this and uncertainty factors such as large perturbation in the core center, the composition ratio of the material, and self-shielding of the foil can affect the accuracy in the calculation and in the measurement.

Table 5 – Measured and calculated subcriticality values for Case III cores.

Configuration	Inserted rods (fully inserted)	Experiment (%Δρ)	Calculation (%Δρ)	Relative error (%)
Case III-1	C1, C2, C3	−0.850 ± 0.060	−0.844 ± 0.008	0.8
Case III-2	C1, C2, C3, S4, S5, S6	−1.751 ± 0.123	−1.614 ± 0.009	7.8
Case III-3	C1, C2, C3, S5, S6	−1.223 ± 0.086	−1.142 ± 0.009	6.6

Table 6 – The Calculation/Experiment values for the foil activation calculation in the target region.

Reaction	Threshold (MeV)	ENDF/B-VII.1 continuous energy cross-section library	IRDFFv1.05 dosimetry library	JENDL/D-99 dosimetry library
$^{115}In(n,n')^{115m}In$	0.32	1.21 ± 0.02	0.93 ± 0.02	0.88 ± 0.01
$^{56}Fe(n,p)^{56}Mn$	2.97	0.37 ± 0.01	1.10 ± 0.02	1.09 ± 0.02
$^{27}Al(n,\alpha)^{24}Na$	3.25	0.37 ± 0.01	1.10 ± 0.02	1.10 ± 0.02
$^{93}Nb(n,2n)^{92m}Nb$	9.05	0.94 ± 0.02	0.94 ± 0.02	0.94 ± 0.02

Al, aluminum; Fe, iron; In, indium; Mn, manganese; Na, sodium; Nb, niobium.

Table 7 – The Calculation/Experiment (C/E) values for the foil activation calculation in the core region.

Case	Subcriticality (%Δρ)	Reaction	ENDF/B-VII.1 continuous energy cross-section library	IRDFFv1.05 dosimetry library	JENDL/D-99 dosimetry library
III-1	0.85	^{115}In(n,n')^{115m}In	2.68 ± 0.07	0.56 ± 0.01	0.55 ± 0.01
		^{56}Fe(n,p)^{56}Mn	0.16 ± 0.01	0.16 ± 0.01	0.16 ± 0.01
		^{27}Al(n,α)^{24}Na	1.03 ± 0.03	1.02 ± 0.03	1.02 ± 0.03
III-2	1.75	^{115}In(n,n')^{115m}In	3.15 ± 0.07	0.65 ± 0.01	0.65 ± 0.01
		^{56}Fe(n,p)^{56}Mn	0.25 ± 0.01	0.25 ± 0.01	0.25 ± 0.01
		^{27}Al(n,α)^{24}Na	0.93 ± 0.02	0.93 ± 0.02	0.93 ± 0.02
III-3	1.22	^{115}In(n,n')^{115m}In	6.44 ± 0.14	1.34 ± 0.03	1.33 ± 0.03
		^{56}Fe(n,p)^{56}Mn	0.37 ± 0.01	0.38 ± 0.01	0.37 ± 0.01
		^{27}Al(n,α)^{24}Na	1.92 ± 0.05	1.90 ± 0.05	1.91 ± 0.05
		^{93}Nb(n,2n)^{92m}Nb	2.18 ± 0.12	0.74 ± 0.04	0.74 ± 0.04

Al, aluminum; Fe, iron; In, indium; Mn, manganese; Na, sodium; Nb, niobium.

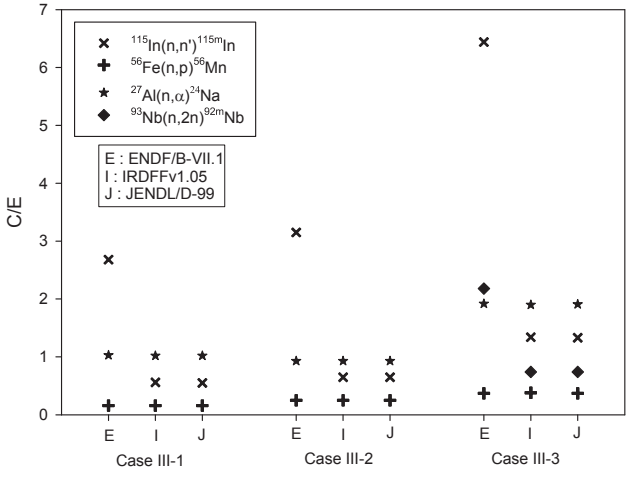

Fig. 22 – The Calculation/Experiment (C/E) values for the foil activation calculation in the core region.

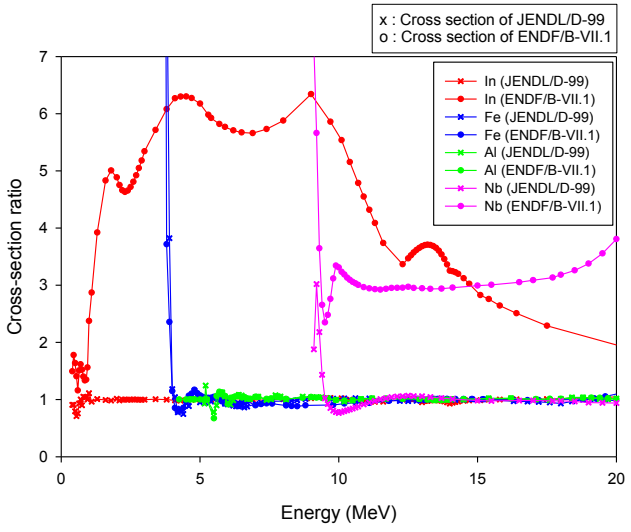

Fig. 23 – Comparison of the cross-sections with respect to the IRDFFv1.05 library. Al, aluminum; Fe, iron; In, indium; Nb, niobium.

This work presents a comparative analysis and new reference solution for the KUCA ADS benchmark with the latest nuclear data libraries (i.e., ENDF/B-VII.1 and IRDFFv1.05).

Conflicts of interest

All authors have no conflicts of interest to declare.

Acknowledgements

This work was supported by a grant from the National Research Foundation of Korea (Seoul, Korea) funded by the Korean government (Ministry of Science, ICT, and Future Planning; Seoul, Korea; grant no. NRF-2014M2A8A2074455). This work was supported by the Nuclear Power Core Technology Development Program of the Korea Institute of Energy Technology Evaluation and Planning (Seoul, Korea) and granted financial resource by the Ministry of Trade, Industry and Energy, Republic of Korea (Sejong City, Korea; grant no. 20141520400090).

REFERENCES

[1] T. Stefan, Evaluation of accelerator-driven subcritical systems for transmutations of nuclear waste, Int. J. Energy Res. 24 (2000) 935–951.
[2] H.A. Abderrahim, Multi-purpose Hybrid Research Reactor for High-tech applications a multipurpose fast spectrum research reactor, Int. J. Energy Res. 36 (2012) 1331–1337.
[3] C.H. Pyeon, Experimental Benchmarks for Accelerator-Driven System (ADS) at Kyoto University Critical Assembly (KUCA), KURRI-TR-444, Kyoto University, Kyoto (Japan), 2007.
[4] C.H. Pyeon, Y. Hirano, T. Misawa, H. Unesaki, C. Ichihara, T. Iwasaki, S. Shiroya, Preliminary experiments on accelerator-driven subcritical reactor with pulsed neutron generator in Kyoto University Critical Assembly, J. Nucl. Sci. Technol. 44 (2007) 1368–1378.
[5] J.T. Goorley, M. James, T. Booth, F. Brown, J. Bull, L.J. Cox, J. Durkee, J. Elson, M. Fensin, R.A. Forster, J. Hendricks, Initial MCNP6 Release Overview—MCNP6 version 1.0. Los Alamos National Laboratory Report, LA-UR-13-22934, Los Alamos National Laboratory, Los Alamos (NM), 2013.
[6] H. Aybaba, Determining of energy multiplication in the APEX hybrid reactor by using THF_4 and UF_4 heavy metal salts, Int. J. Energy Res. 36 (2012) 1375–1382.

[7] M.B. Chadwick, M. Herman, P. Obložinský, M.E. Dunn, Y. Danon, A.C. Kahler, D.L. Smith, B. Pritychenko, G. Arbanas, R. Arcilla, R. Brewer, ENDF/B-VII.1 nuclear data for science and technology: cross sections, covariances, fission product yields and decay data, Nucl. Data Sheets 112 (2011) 2887–2996.
[8] R. Capote, K.I. Zolotarev, V.G. Pronyaev, A. Trkov, Updating and extending the IRDF-2002 Dosimetry Library, J. ASTM Int. 9 (2012) 197–209.
[9] K. Kobayashi, T. Iguchi, S. Iwasaki, JENDL Dosimetry File 99 (JENDL/D-99), JAERI Report 1344, Japan Atomic Energy Research Institute, Tokyo (Japan), 2002.
[10] C.H. Pyeon, H. Shiga, T. Misawa, T. Iwasaki, S. Shiroya, Reaction rate analyses for an accelerator-driven system with 14 MeV neutrons in the Kyoto University Critical Assembly, J. Nucl. Sci. Technol. 46 (2009) 965–972.
[11] C.H. Pyeon, M. Hervault, T. Misawa, H. Unesaki, T. Iwasaki, S. Shiroya, Static and kinetic experiments on accelerator-driven system in Kyoto University Critical Assembly, J. Nucl. Sci. Technol. 45 (2008) 1171–1182.
[12] M. Tesinsky, C. Berglöf, T. Bäck, B. Martsynkevich, I. Serafimovich, V. Bournos, A. Khilmanovich, Y. Fokov, S. Korneev, H. Kiyavitskaya, W. Gudowski, Comparison of calculated and measured reaction rates obtained through foil activation in the subcritical dual spectrum facility YALINA-Booster, Ann. Nucl. Energy 38 (2011) 1412–1417.
[13] C.H. Pyeon, Y. Takemoto, T. Yagi, J.Y. Lim, Y. Takahashi, T. Misawa, Accuracy of reaction rates in the accelerator-driven system with 14 MeV neutrons at the Kyoto University Critical Assembly, Ann. Nucl. Energy 40 (2012) 229–236.